Velocity oscillations in turbulent Rayleigh–Bénard convection

X.-L. Qiu
Department of Physics, Oklahoma State University, Stillwater, Oklahoma 74078

X.-D. Shang
Department of Physics, The Chinese University of Hong Kong, Shatin, Hong Kong

P. Tong
Department of Physics, Oklahoma State University, Stillwater, Oklahoma 74078
and Department of Physics, Hong Kong University of Science and Technology, Clear Water Bay, Kowloon, Hong Kong

K.-Q. Xia
Department of Physics, The Chinese University of Hong Kong, Shatin, Hong Kong

(Received 24 February 2003; accepted 5 November 2003; published online 7 January 2004)

A systematic study of velocity oscillations in turbulent thermal convection is carried out in small aspect-ratio cells filled with water. Local velocity fluctuations and temperature-velocity cross-correlation functions are measured over varying Rayleigh numbers and spatial positions across the entire convection cell. These structural measurements reveal how the thermal plumes interact with the bulk fluid in a closed cell and provide an interesting physical picture for the dynamics of the temperature and velocity oscillations in turbulent convection. © *2004 American Institute of Physics.* [DOI: 10.1063/1.1637350]

I. INTRODUCTION

Turbulent Rayleigh–Bénard convection is an interesting problem in nonlinear physics and has attracted much attention in recent years.[1–4] Despite its relatively low Reynolds number (Re), turbulent convection shares many common features that are usually associated with high-Re turbulent flows. These features include coherent structures, intermittent fluctuations, and anomalous scaling. There are two coherent structures, which are found to coexist in the convection cell. One is the large-scale circulation that spans the height of the cell, and the other is intermittent bursts of thermal plumes from the upper and lower thermal boundary layers. An intriguing feature of turbulent convection is the emergence of a well-defined low-frequency oscillation in the temperature power spectrum.[1,5] This oscillation takes place in the hard turbulence regime when the Rayleigh number (Ra) becomes larger than a critical value Ra_c ($\mathrm{Ra}_c \simeq 5\times 10^7$ in the aspect-ratio-one cell). Recent velocity measurements[6–8] found a similar oscillation in the velocity power spectrum. The temperature and velocity oscillations have been observed in various convecting fluids, including low temperature helium gas,[1,5] sulfur hexafluoride gas near its critical point,[6] mercury,[9,10] and water.[7,8,11] These measurements have stimulated considerable theoretical efforts, aimed at explaining the dynamic origin of the temperature oscillation.[1,5,10,12]

In an attempt to further understand the structure and dynamics of the thermal plumes, we have recently carried out a systematic study of the temperature and velocity fields in turbulent convection.[13,14] Using the techniques of laser Doppler velocimetry (LDV), thermometry, and flow visualization, we map out the temperature and velocity structures in the plane of the large-scale circulation. The temperature and velocity measurements are conducted in convection cells with different aspect ratios and over varying Rayleigh numbers and spatial positions across the entire cell. Water is used as the convecting fluid, in which the temperature and velocity measurements can be made simultaneously with high accuracy. These local measurements provide a body of reliable velocity and temperature data and complement the global measurements of heat transport in turbulent convection.[1,15–19]

In Ref. 14 (and a rapid communication[20]), we have described the structure of the temperature field in turbulent convection. Direct measurements of local temperature fluctuations and their spatial correlation functions are carried out at various Rayleigh numbers and spatial positions. These measurements fully characterize the spatial structure of the temperature oscillation and reveal interesting dynamics of the thermal plumes near the conducting surface. A sharp transition from a random chaotic state to a correlated turbulent state of finite coherence time is found in the aspect-ratio-one cell when Ra becomes larger than $\mathrm{Ra}_c \simeq 5\times 10^7$. Above Ra_c the measured temperature correlation functions show a well-defined oscillation with a finite coherence time. The oscillation period is found to be twice as large as the measured transit time for the thermal plumes to travel between the upper and lower conducting surfaces (cell crossing time). The measurements demonstrate that the thermal plumes in a closed cell organize themselves both in space and time, which provides a unique driving mechanism for the temperature oscillation in turbulent convection.

The experiment is in good agreement with Villermaux's theory,[12] which proposed that the temperature oscillation is caused by a thermal boundary layer instability triggered by

the incoming thermal plumes from the opposite conducting surface. These thermal plumes are transported by the large-scale circulation having a mean velocity U. Villermaux's model assumed that the unstable modes (i.e., the thermal plumes) in the upper and lower thermal boundary layers interact through a delayed nonlinear coupling with a time constant equal to the cell crossing time $t_0 \simeq L/U$, where L is the cell height. Because of this delayed coupling, the thermal plumes are excited alternately between the upper and lower boundary layers with a local frequency $f_0 = 1/(2t_0) \simeq U/(2L)$.

An important question one might ask is how is the temperature oscillation related to the velocity oscillation observed in the same convection cell? While Villermaux's model explained the dynamic origin of the temperature oscillation, it did not discuss the consequences of the alternating emission of thermal plumes to the flow field. In this paper we focus our attention on the correlation between the velocity and temperature fields in turbulent convection. Simultaneous measurements of the local flow velocity and temperature are carried out using the techniques of LDV and thermometry. From these measurements we obtain the temperature–velocity cross-correlation function over varying Rayleigh numbers and spatial positions across the entire cell. The simultaneous velocity and temperature measurements fully characterize the spatial structure of the velocity oscillation and allow us to answer some important open questions that are related directly to the physical understanding of convective turbulence. These questions include: How is the velocity oscillation generated and sustained? What is the connection between the velocity oscillation and the coherent structures in the flow, such as the large-scale circulation and the thermal plumes? The experiment demonstrates that turbulent convection in a closed cell is a well organized flow and the structural measurements are essential to the physical understanding of convective turbulence.

The remainder of the paper is organized as follows. We first describe the apparatus and the experimental method in Sec. II. Experimental results are discussed in Sec. III. Finally, the work is summarized in Sec. IV.

II. EXPERIMENT

The experiment is conducted in two up-right cylindrical cells filled with water. The height of the larger cell is 20.4 cm and its inner diameter is 19.0 cm. The smaller cell is 8.2 cm in height and 8.2 cm in inner diameter. The corresponding aspect ratio A (=diameter/height) of these cells is unity. The sidewall of the cells is made of a transparent Plexiglas ring with wall thickness 0.6 cm. The top and bottom plates are made of brass and their surfaces are electroplated with a thin layer of gold. The thickness of the top plate is 1.0 cm and that of the bottom plate is 0.85 cm. The Plexiglas ring is sandwiched between the two plates and is sealed to the top and bottom plates via two regular rubber O rings. The top and bottom plates together with the sidewall are held together by six Teflon posts evenly spaced on a circle slightly larger than the outer diameter of the Plexiglas ring. Two silicon rubber film heaters connected in parallel are sandwiched on the backside of the bottom plate to provide constant and uniform heating. A dc power supply with a 99.99% long-term stability is used to provide the heating power. The voltage applied to the heaters varies from 20 to 90 V, and the corresponding heating power is in the range between 24 and 485 W. The upper side of the top plate is in good contact with a cooling chamber, whose temperature is maintained constant by circulating cold water from a temperate-controlled bath/circulator. The temperature stability of the circulator is 0.01 °C. Cold water is fed into the chamber through two opposing inlets on the side of the chamber and flows out through two outlets on the top of the chamber.

To record the temperature of the conducting plates, we embed two thermistors beneath the surface of each plate. One thermistor is located at the center of the plate and the other is placed half way between the plate center and the sidewall. The whole convection cell (except an optical window) is wrapped in three layers of thermal insulating rubber sheets to prevent heat leakage. In the experiment, the temperature difference ΔT between the top and bottom plates varies from 4 to 51 °C depending on the heating power. By adjusting the temperature of the cooling water, we maintain the temperature of the bulk fluid at ~29 °C for all the measurements. The corresponding Prandtl number (Pr) of the fluid is approximately 5.4. The temperature stability of the top and bottom plates is found to be within 0.1 °C in standard deviation, which is less than 2.5% of the minimum ΔT used in the experiment.

The two $A=1$ cells are used to extend the accessible range of the Rayleigh number $\mathrm{Ra} = \alpha g \Delta T L^3/(\nu\kappa)$, where g is the gravitational acceleration, L is the cell height, and α, ν, and κ are, respectively, the thermal expansion coefficient, the kinematic viscosity, and the thermal diffusivity of the convecting fluid (water). The larger cell covers the Ra range between 7.5×10^8 and 1×10^{10}, and the smaller cell covers the Ra range between 1.75×10^7 and 7.1×10^8. For the highest Ra ($=7.1\times10^8$) in the smaller cell, we have $\Delta T = 50.9$ °C and the non-Boussinesq temperature deviation, defined as $\Delta_c \equiv T_c - (T_b + T_t)/2$, is found to be $\Delta_c = 2.9$ °C, where T_c is the average temperature of the bulk fluid measured at the cell center, and T_b and T_t are the average temperature of the bottom and top plates, respectively. Thus we have $\Delta_c/\Delta T \simeq 5.7\%$. When the Boussinesq approximation is valid, Δ_c is expected to be zero.[21] In the larger cell at Ra $=1.5\times10^9$, we have $\Delta T = 8.0$ °C, $\Delta_c = 0.4$ °C, and the corresponding ratio $\Delta_c/\Delta T = 5\%$. When compared with the non-Boussinesq temperature deviations in glycerol,[22] we find the values of Δ_c in water are smaller. However, we have not yet studied any non-Boussinesq effect in our system systematically. To check the aspect-ratio dependence, we also use two other cells with $A=2$ and $A=0.5$, respectively. These two cells have the same inner diameter of 19.0 cm but their height is different; one is 9.5 cm and the other is 40.7 cm.

Figure 1(a) shows the experimental arrangement for the velocity and temperature measurements. Local velocity measurements are conducted using a two-component LDV system (TSI Inc.) together with an argon-ion laser (Coherent Innova 90). A long rectangular flat window (W) made of transparent Plexiglas with wall thickness 0.6 cm is inserted

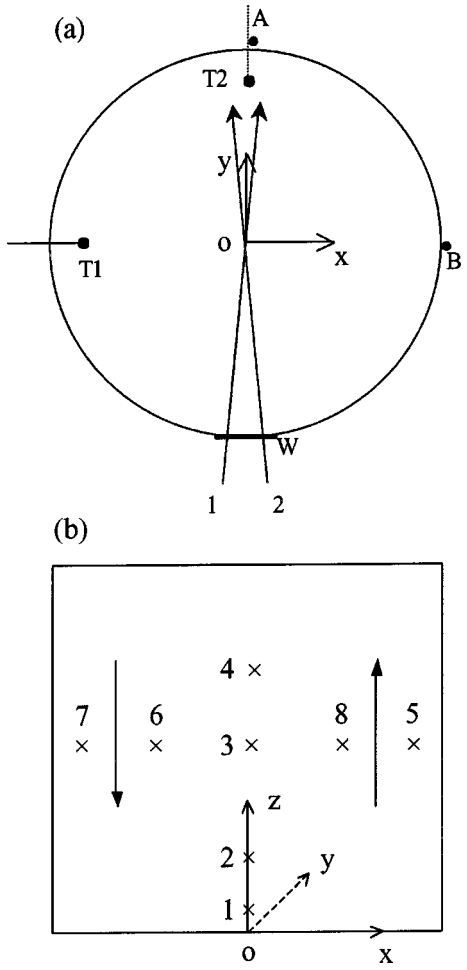

FIG. 1. (a) Schematic diagram of the experimental setup (top view): T1, T2, temperature probes; 1, 2, two laser beams for LDV; W, optical window. (b) Space coordinates and eight locations for the velocity and temperature measurements. The long arrows near the sidewall indicate the direction of the large-scale circulation.

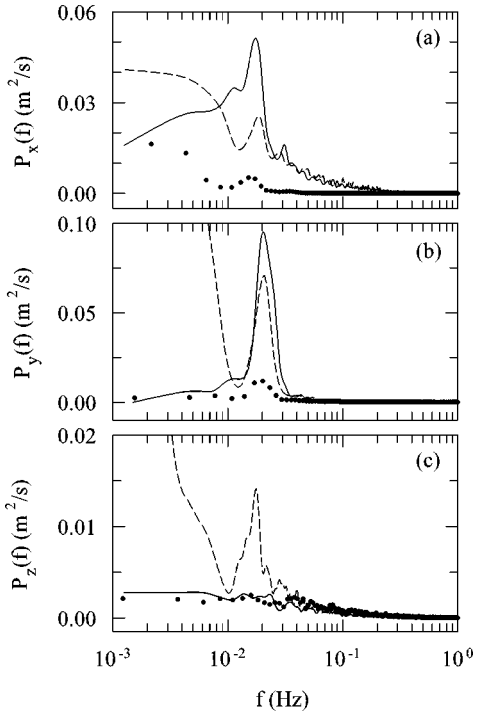

FIG. 2. Measured frequency power spectra (a) $P_x(f)$, (b) $P_y(f)$, and (c) $P_z(f)$ for v_x, v_y, and v_z, respectively, at Ra$=3.7\times10^9$. (a) The measurements are made along the central z axis at positions 1 ($z=9$ mm, dotted curve), 2 ($z=42$ mm, dashed curve), and 3 ($z=102$ mm, solid curve). (b) The measurements are made at positions 1 (dashed curve), 3 (solid curve), and 5 (8 mm away from the sidewall, dotted curve). (c) The measurements are made at positions 1 ($z=20$ mm, dotted curve), 3 (solid curve), and 5 (15 mm away from the sidewall, dashed curve).

onto the sidewall of the cell to admit the incident laser beams and observe the scattered light by seed particles. The width of the optical window is 3 cm for the larger cell and 1.5 cm for the smaller cell. The length of the optical window remains the same as the height of the Plexiglas ring. Two pairs of laser beams of different color (blue and green) coming from a LDV fiberoptic transceiver are directed through the optical window and focused onto a single point inside the convection cell. The fiberoptic transceiver has a receiving fiber, which collects the scattered light in the backward direction and feeds it to two photomultiplier tubes (one detects the blue light and the other detects the green light). The laser focusing spot has a cylindrical probe volume of 1.31 mm in length and 0.09 mm in diameter. The two laser beams shown in Fig. 1(a) are in the horizontal plane and are used to measure the horizontal velocity v_x in the x direction. The other two laser beams (not shown) are in the vertical plane parallel to the laser propagation direction. These two beams are used to measure the vertical velocity v_z along the z axis.

Monodisperse polymer latex spheres of 4.75 μm in diameter are used as seed particles. Because their density (1.05 g/cm^3) matches closely to that of water, the seed particles follow the local flow well. In the experiment, we measure the local velocity as a function of time and the measuring position (laser focusing spot) can be varied continuously along the y axis (horizontal scan) and the z axis (vertical scan). This is accomplished by moving the fiberoptic transceiver, which is mounted on a traversable table. A typical sampling rate of the velocity measurements is 10–15 Hz, which is approximately 10 times larger than the cutoff frequency of the velocity power spectrum. Typically, we take 7-h-long time series data ($\sim5\times10^5$ data points) at each position. The data accumulation time is much longer than the time scale for the large-scale circulation, which is of the order of 1 min (see Fig. 2 for more details), ensuring that the statistical average of the flow properties is adequate.

In this way, we obtain a complete series of velocity data at various Rayleigh numbers and spatial locations with the highest statistical accuracy possible. In the calculation of the velocity statistics, we use the transit time weighting to correct for the velocity sampling bias.[23] The velocity power spectrum is obtained using a software package provided by TSI Inc. With unevenly sampled velocity time series data $v(t)$, the program calculates the autocorrelation function of $v(t)$ first and then Fourier-transforms the autocorrelation function back to the frequency domain. As a result, the obtained velocity power spectrum becomes sensitive to the mean flow (extra-low frequency component). In the data

analysis to be discussed below, we will ignore this low-frequency tail.

Simultaneous velocity and temperature measurements are carried out using a multichannel LDV interface module (TSI Datalink) to synchronize the data acquisition. A triggering pulse from the LDV signal processor initiates the acquisition of an analog temperature signal. A small movable thermistor (T1 or T2) of 0.2 mm in diameter, 15 ms in response time, and 1 mK/Ω in temperature sensitivity (Thermometrics, AB6E3-B10KA202J) is used to measure the local fluid temperature. To guide the thermistor into the cell, we install a horizontal stainless steel tube on the sidewall. The stainless steel tube (Type 304 SS hypodermic tubing) has an outer diameter of 1.07 mm and wall thickness of 0.19 mm. Thin thermistor wires thread through the stainless steel tube from the outside and a small head piece of the sensor tip sticks out of the tube end inside the convection cell. The tube end together with the sensor tip is sealed with glue so that the convecting fluid cannot leak out through the stainless steel tube.

The horizontal tube can be mounted at three different heights on the sidewall. At a given height the tube can slide in and out so that the local fluid temperature $T_i(t)$ (here i is used to indicate the probe position) can be measured at various horizontal positions away from the sidewall. The thermistor is connected to an ac bridge as a resistance arm. The voltage signals from the ac bridge are fed to the interface module, whose output is connected to the LDV signal processor. A host computer is used to store each pair of the velocity and temperature measurements with the same time stamp. All the thermistors used in the experiment are calibrated individually with an accuracy of 0.01 °C. In the experiment, we also vary the spatial separation between the laser focusing spot and the thermistor tip.

Figure 1(b) shows the space coordinates to be used below in the presentation of the velocity and temperature measurements. The origin of the coordinate system is chosen to coincide with the center of the lower conducting surface. The x and z axes are in the rotation plane of the large-scale circulation (LSC) and the y axis is perpendicular to the rotation plane. It has been shown[24] that the extent of LSC in the y direction may vary between 2/3 and 1/3 of the cell diameter when Ra is in the range $5\times10^9<\mathrm{Ra}<10^{10}$ (in the $A=1$ cell). The eight crosses shown in Fig. 1(b) indicate the locations of the velocity and temperature measurements made in the rotation plane. Early temperature measurements[10] showed that the azimuth of LSC rotates slowly in time when the cylindrical cell is levelled perfectly. It was found recently that LSC in the levelled cylindrical cell also reverses its rotational direction randomly.[25,26] The reversal of LSC occurs suddenly in a time span much less than a rotation period, whereas the typical duration between two successive reversals remains quite long when compared with the rotation period (more than 10 rotation periods).

To pin down the azimuthal rotation and the random reversal of LSC, we tip the cell with a small angle ($<1°$) by adding a few sheets of paper on one side of the cell bottom. Ciliberto *et al.*[11] have shown that such a small tilt does not affect turbulent convection very much. When we tip the cell at position B [see Fig. 1(a)], LSC is setup in the $x-z$ plane and the direction of rotation is shown in Fig. 1(b). In this case, the LDV setup shown in Fig. 1(a) is capable of measuring the two in-plane velocity components v_x and v_z. One can also tip the cell at position A and setup LSC in the $y-z$ plane. In this case, we can measure the in-plane velocity component along the mean flow direction and an out-of-plane velocity component perpendicular to the rotation plane of LSC. To avoid confusion, hereinafter we choose the $x-z$ plane to coincide with the rotation plane of LSC regardless of the actual arrangement of the tilt.

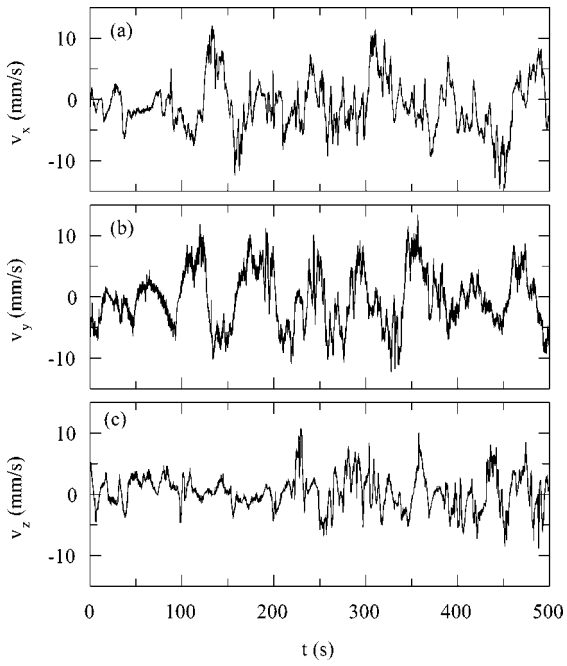

FIG. 3. Time series measurements of velocity fluctuations at the cell center. The measurements are made at $R=3.7\times10^9$ and the three velocity components are (a) v_x, (b) v_y, and (c) v_z.

III. RESULTS AND DISCUSSION

A. Spatial structure of velocity oscillations

Figure 2 shows the measured frequency power spectra $P_x(f)$, $P_y(f)$, and $P_z(f)$ for the three velocity components v_x, v_y, and v_z, respectively. The measurements are made at various locations in the central core region, near the sidewall, and near the lower conducting surface. A sharp peak at $f_0=0.018\pm0.002$ Hz is found in all the horizontal power spectra, $P_x(f)$ and $P_y(f)$, measured at different locations. From the height of the frequency peak we find that the horizontal velocities at the cell center oscillate with a much larger amplitude than those around the cell periphery. At the cell center, the measured $P_y(f)$ has a larger frequency peak when compared with $P_x(f)$. Contrary to the horizontal power spectra, the vertical power spectrum $P_z(f)$ shows a sharp frequency peak only in the sidewall region. In the central region v_z fluctuates randomly and no obvious frequency peak is found in the measured $P_z(f)$.

Figure 3 shows the time series measurements of the three velocity components v_x, v_y, and v_z at the cell center.

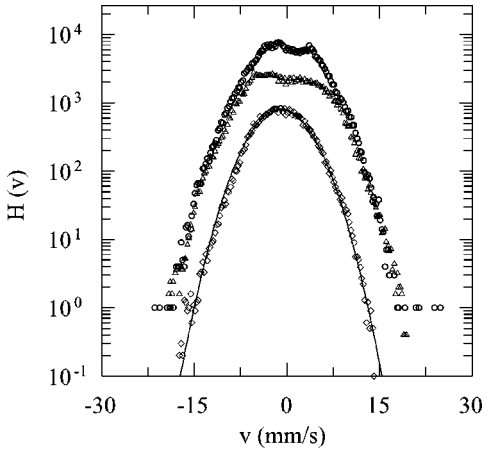

FIG. 4. Corresponding velocity histograms $H(v_x)$ (circles), $H(v_y)$ (triangles), and $H(v_z)$ (diamonds) for the time series data shown in Fig. 3. The solid curve shows a Gaussian fit to the diamonds. For clearness, the origin of the lower two curves is shifted downwards.

Clear oscillations are observed only in the two horizontal components but not in the vertical component. The horizontal velocity v_y perpendicular to the rotation plane of LSC exhibits the strongest coherent oscillation. It is found that the velocity oscillations in different directions and at various locations all have the same frequency at a fixed Ra, suggesting that they are driven by a common mechanism. As will be shown in Fig. 12 below, the velocity oscillation frequency f_0 varies with both Ra and the cell height L and its numerical value is the same as that of the temperature oscillation.

Figure 4 shows the corresponding velocity histograms $H(v_x)$ (circles), $H(v_y)$ (triangles), and $H(v_z)$ (diamonds) at the cell center. It is seen that the measured $H(v_z)$ can be well described by a Gaussian function (solid curve) over an amplitude range of almost 4 decades. The measured $H(v_x)$ and $H(v_y)$ are also of Gaussian shape but they exhibit two small bumps near the zero mean. This is caused by the horizontal oscillations discussed above.

In Ref. 13 we have described the detailed structure of the mean velocity field in turbulent convection. Large velocity fluctuations are found both in the central region and near the cell boundary. Despite the large velocity fluctuations, the flow field still maintains a coherent structure. Figure 5 shows a sketch of the velocity field in an aspect-ratio-one cell. This picture is derived from that shown in Ref. 4 but is modified with inputs from our recent experiments.[13,14] The flow field has a quasi-two-dimensional structure, which undergoes a coherent rotation. The single-roll structure shown in Fig. 5 can be divided into three regions in the rotation plane: (i) a thin viscous boundary layer around the cell periphery, (ii) a fully mixed central core region of size $\sim L/2$, and (iii) an intermediate plume-dominated buffer layer of thickness $\sim L/4$. The plume-dominated buffer layer is the active region that drives the large-scale circulation. Thermal plumes erupt into the region from the upper and lower thermal boundary layers and are separated laterally in the two opposing sidewall regions. The warm and cold plumes exert buoyancy forces on the fluid and drive the vertical rising and falling flows near the sidewall. The central core region is ''sheared''

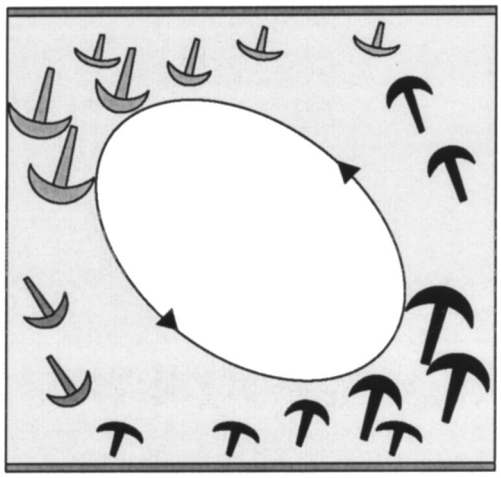

FIG. 5. A schematic drawing of the velocity field and the plume distribution in the aspect-ratio-one cell. The central core region (unshaded) is the fully mixed bulk region and the shaded area shows the plume-dominant region. The thin layers with wiggly lines near the upper and lower surfaces indicate the thermal boundary layers. Cold plumes (light colored) fall on the left side of the cell and warm plumes (dark colored) rise on the right side of the cell. The arrows indicate the direction of the large-scale circulation.

by the rising and falling plumes, resulting in a constant mean velocity gradient in the region.

Figure 6(a) shows how the large-scale flow v_z near the sidewall changes with time. It is seen that the large-scale flow oscillates mainly in one direction, staying at a large velocity ($\sim$18 mm/s) for a while and then falling to a minimum velocity (close to 0) momentarily. This asymmetric os-

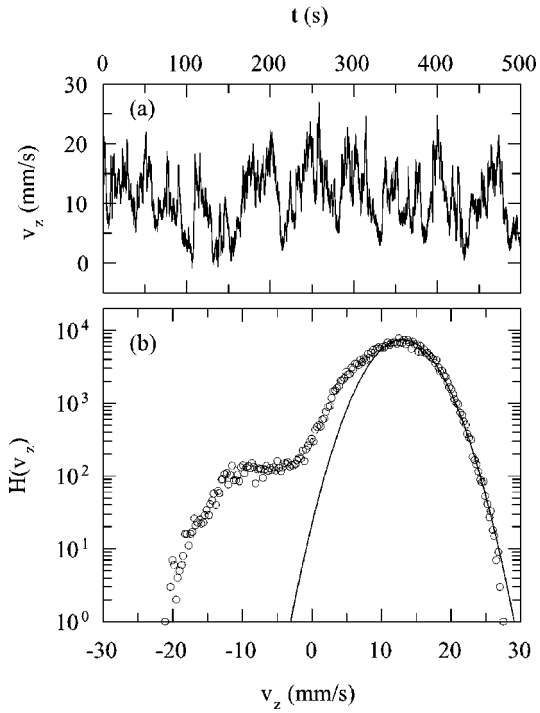

FIG. 6. (a) Time series measurements of the vertical velocity v_z at Ra $=3.7\times10^9$. The measurements are made at position 5 (8 mm away from the sidewall). (b) Corresponding velocity histogram $H(v_z)$. The solid curve is a Gaussian function with mean velocity $\overline{v_z}=13.0$ mm/s and standard deviation $\sigma_z=3.8$ mm/s.

cillation gives rise to a large mean vertical velocity ($\sim$13 mm/s) in the sidewall region. Figure 6(b) shows the corresponding velocity histogram $H(v_z)$. Contrary to the Gaussian distribution at the cell center, the measured $H(v_z)$ near the sidewall shows a bimodal distribution with a dominant peak at a positive velocity and a secondary peak at a negative velocity, whose absolute value is comparable to that of the main peak. It is also seen that the main peak is adequately described a Gaussian function (solid curve) and the secondary peak is approximately 60 times smaller than the main peak.

We find that the measured $H(v_z)$ deviates from the Gaussian shape gradually and becomes more and more asymmetric when the measuring point is moved away from the cell center. The histogram is skewed against the mean flow, having the largest skewness at the edge of the velocity boundary layer, at which the mean flow velocity reaches maximum. The measured histograms at other Rayleigh numbers and in the $A=0.5$ cell are similar to that shown in Fig. 6(b). Careful examination of the time series data near the sidewall reveals that contributions to the secondary peak come mainly from occasional negative spikes in the velocity signals. These negative spikes last only 5–10 s (less than half of the rotation period) and should not be confused with the random reversal of LSC. As mentioned in Sec. II, the reversal of LSC has a much longer time span (more than 10 rotation periods) than these short velocity spikes. We have verified that when the cell is tilted, the direction of the mean flow remains unchanged during the entire experiment. We believe that the negative velocity spikes are caused by a small number of energetic cold plumes, which erupt from the upper conducting surface and move downward against the rising mean flow at position 5. Because thermal plumes erupt alternately between the upper and lower boundary layers, the cold plumes fall in the ''quiet'' time period between two consecutive bursts of rising warm plumes at position 5. These events are rare because most cold plumes move downward on the other side of the cell (position 7).

We also study the velocity oscillation in the $A=2$ and $A=0.5$ cells. Figure 7(a) shows the measured $P_x(f)$ (upper solid curve), $P_y(f)$ (dashed curve), and $P_z(f)$ (lower solid curve) at the center of the $A=2$ cell. The measurements are made at Ra$=4.9\times10^8$. Clear oscillations are observed in all three velocity components. Figure 7(b) compares the measured $P_x(f)$ in the $A=2$ cell (dotted curve) with that in the $A=1$ cell (solid curve) at a similar Rayleigh number (Ra $=4.7\times10^8$). It is seen that the amplitude of the frequency peak in the $A=2$ cell is approximately two orders of magnitude larger than that in the $A=1$ cell, suggesting that the velocity oscillations in the $A=2$ cell are much stronger. In fact, one can observe the velocity oscillations directly from the time series data. Note that the frequency peak in the $A=1$ cell can still be identified clearly at this Rayleigh number, as shown in the inset of Fig. 7(b).

Figure 8 shows the measured frequency power spectra at the center of the $A=0.5$ cell. The measurements are made at Ra$=3.1\times10^{10}$. Contrary to the results obtained in the $A=1$ and $A=2$ cells (at somewhat smaller Rayleigh numbers), no obvious frequency peak is found in the power spectra measured in the $A=0.5$ cell. This conclusion is further confirmed by the measurements at another Rayleigh number (Ra$=5.8\times10^{10}$) in the same hard turbulence regime. In an early convection experiment with low temperature helium gas,[27] Wu and Libchaber also reported that the temperature oscillation is absent in the $A=0.5$ cell.

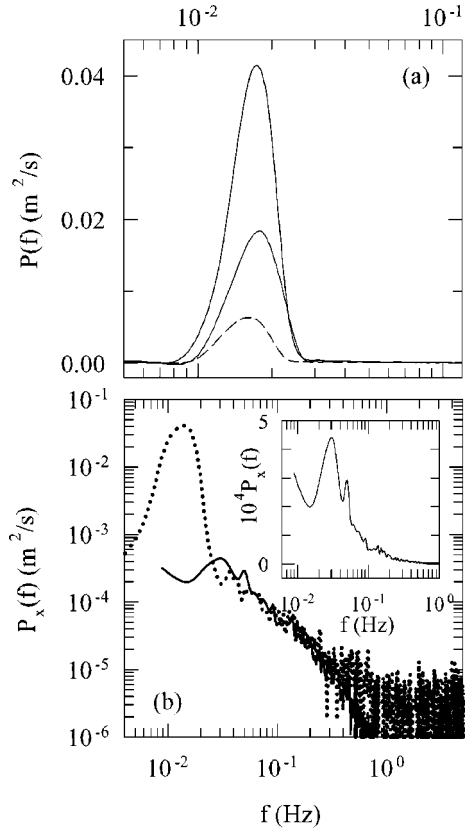

FIG. 7. (a) Measured frequency power spectra $P_x(f)$ (upper solid curve), $P_y(f)$ (dashed curve), and $P_z(f)$ (lower solid curve) at Ra$=4.9\times10^8$. The measurements are made at the center of the $A=2$ cell. (b) Comparison between the measured $P_x(f)$ in the $A=1$ cell at Ra$=4.7\times10^8$ (solid curve) and in the $A=2$ cell at Ra$=4.9\times10^8$ (dotted curve). Inset shows a linear plot of $P_x(f)$ vs $\log f$ for the same data obtained in the $A=1$ cell at Ra $=4.7\times10^8$. All the measurements are made at the cell center.

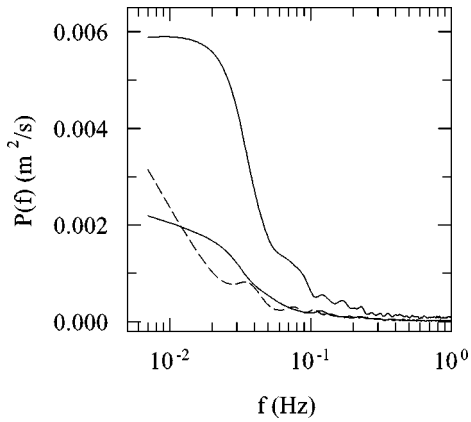

FIG. 8. Measured frequency power spectra $P_x(f)$ (lower solid curve), $P_y(f)$ (dashed curve), and $P_z(f)$ (upper solid curve) at Ra$=3.1\times10^{10}$. The measurements are made at the center of the $A=0.5$ cell.

Villermaux[12] pointed out that the underlying mechanism for the temperature oscillation in a closed convection cell relies on the interplay between the linear growth of primary instability disturbances (i.e., thermal plumes) and the delay of nonlinear saturation due to the finite large-scale velocity U. Therefore, the interaction between the upper and lower thermal boundary layers is critically dependent on the delay time $t_0 \simeq L/U$. It is assumed in Villermaux's model that for a fixed Ra, t_0 does not fluctuate. As a result, the calculated temperature oscillation has an infinite coherence time. As shown in Fig. 6(a), the measured U is actually a fluctuating quantity and thus we have $\delta t_0/t_0 = \delta U/U \simeq \sigma_z/\overline{v_z}$, where $\overline{v_z}$ and σ_z are, respectively, the mean and rms velocities near the sidewall. Fluctuations in the delay time t_0 will broaden the frequency peak at f_0.[12]

Our recent velocity measurements[13] showed that the large-scale flow in the $A=1$ and $A=2$ cells is fairly stable but the large-scale circulation (LSC) in the $A=0.5$ cell wobbles even when the cell is tipped at a larger angle. The wobbly LSC introduces large fluctuations in t_0, which may destroy the coherent oscillation in the $A=0.5$ cell. The measured $\sigma_z/\overline{v_z}$ in the $A=1$ and $A=2$ cells has a typical value of 0.5, whereas in the $A=0.5$ cell it becomes slightly larger than 1.[13] When the rms velocity becomes larger than the mean value, one will not be able to visualize a persistent large-scale circulation directly. It was also found[13] that the time-averaged large-scale flow in the $A=0.5$ cell has a single role structure similar to that in the $A=1$ cell. Recent velocity measurements by Masaki Sano and co-workers showed that the velocity field in the $A=0.5$ cell filled with mercury (Pr $\simeq 0.024$) has a similar single roll structure (private communication). In the tilted $A=0.5$ cylinder filled with water (Pr $\simeq 5.4$), we did not observe a flow structure with two vertically stacked, aspect-ratio-one rolls, as suggested by recent numerical simulations.[28] The numerical study[28] was carried out in a levelled $A=0.5$ cylinder filled with helium gas (Pr $=0.7$). A transition from a one-roll flow to a two-roll flow was used to explain the observed bimodal behavior of the measured Nusselt number in an $A=0.5$ cell filled with low-temperature helium gas.[29]

From the above velocity measurements together with the recent temperature measurements,[14,20] we arrive at the following physical picture for the velocity oscillation in the $A=1$ cell. As discussed in the above, the temperature oscillation is generated by the alternating emission of cold and warm plumes between the upper and lower thermal boundary layers. These cold and warm plumes are separated laterally in the two opposing sidewall regions and exert buoyancy forces to the surrounding fluid. As a result, the vertical velocity oscillation in the sidewall region is coupled directly to the temperature oscillation. Such a coupling via direct entrainment is expected to become weaker in the central region, where less thermal plumes are present. This conclusion is supported by the experimental observation that the maximum vertical velocity oscillation occurs in the same sidewall region as that for the temperature oscillation.

To further understand the spatial correlation between the temperature and velocity oscillations, especially the interaction between the vertical thermal forcing and the horizontal velocity oscillations in a closed cell, we conduct simultaneous temperature and velocity measurements and obtain the temperature–velocity cross-correlation function at various locations in the cell. In the next section, we discuss the correlation and phase relationship between the temperature and velocity oscillations.

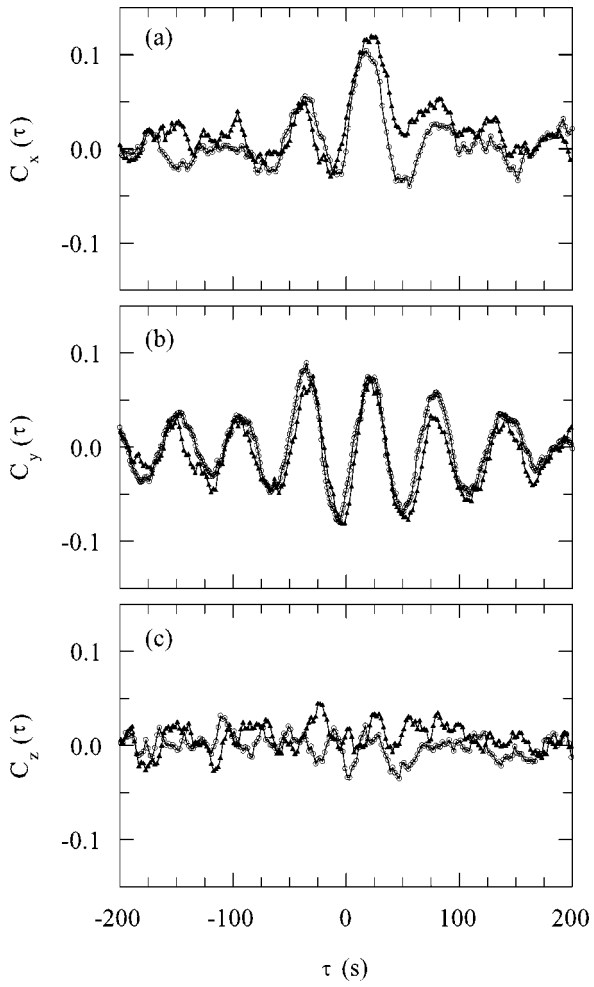

FIG. 9. Measured temperature–velocity cross-correlation functions (a) $C_x(\tau)$, (b) $C_y(\tau)$, and (c) $C_z(\tau)$ as a function of delay time τ at Ra$=3.3\times10^9$. In the experiment the temperature probe is fixed at position 7 (15 mm away from the sidewall) and the velocity measurements are conducted at (a) positions 3 ($z=102$ mm, open circles) and 4 ($z=142$ mm, closed triangles); (b) positions 2 ($z=44$ mm, closed triangles) and 3 (open circles); and (c) positions 4 (closed triangles) and 3 (open circles). The lines are drawn to guide the eye.

B. Correlations between the temperature and velocity oscillations

Figure 9(a) shows the measured temperature–velocity cross-correlation function, $C_x(\tau) = \langle \delta T(t)\, \delta v_x(t+\tau)\rangle / (T_{\rm rms} v_{x({\rm rms})})$, as a function of delay time τ. Here the temperature fluctuation is defined as $\delta T(t) = T(t) - \overline{T}$, where $\overline{T}$ is the mean value of the local temperature $T(t)$, and the velocity fluctuation is defined as $\delta v_x(t) = v_x(t) - \overline{v_x}$, where $\overline{v_x}$ is the mean value of the horizontal velocity $v_x(t)$. The measured $C_x(\tau)$ is normalized by the product of the two standard deviations, $T_{\rm rms}$ and $v_{x({\rm rms})}$. In the experiment the temperature probe is fixed at position 7 and the velocity

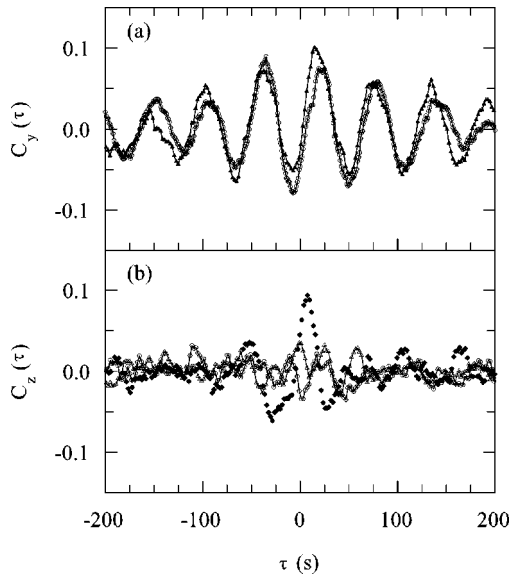

FIG. 10. Measured temperature–velocity cross-correlation functions (a) $C_y(\tau)$ and (b) $C_z(\tau)$ as a function of delay time τ at Ra$=3.3\times10^9$. In the experiment the temperature probe is fixed at position 7 and the velocity measurements are conducted at (a) positions 3 (open circles) and 8 ($x=43$ mm, solid triangles); and (b) positions 3 (open circles), 8 (open triangles), and 6 ($x=-47$ mm, solid diamonds). The lines are drawn to guide the eye.

measurements are made at various locations along the central z axis (vertical scan). Similarly, Figs. 9(b) and 9(c) show the measured $C_y(\tau)$ and $C_z(\tau)$, respectively.

Figure 10 shows the measured $C_y(\tau)$ and $C_z(\tau)$ when the temperature probe is fixed at position 7 and the velocity measurements are made at positions 3, 6, and 8. These three positions are all in the central region of the cell. It has been shown[14,20] that the temperature oscillation takes place mainly in the plume-dominated sidewall region. Using the temperature signals at position 7 as a reference, the cross-correlation functions measure the phase relation between the temperature and velocity oscillations. This phase relation is determined by the delay time of the first maximum (peak) or minimum (valley) position in the cross-correlation function. One can also obtain the phase relation between the velocity oscillations at two different locations by comparing the relative phase difference between the cross-correlation functions measured at the two locations.

Figures 9 and 10 reveal several interesting features of the velocity oscillation in a closed cell. First, while the temperature signals at position 7 show clear oscillations,[14,20] the vertical velocity v_z in the central region fluctuates randomly and no obvious frequency peak is found in the measured $P_z(f)$ [see Figs. 2(c) and 3(c)]. Therefore, one expects that there will be little correlation between $\delta T(t)$ at position 7 and $\delta v_z(t)$ in the central region. This is indeed the case as shown in Figs. 9(c) and 10(b). A small correlation is found only when v_z is measured at a location close to position 7, at which the temperature measurement is made [solid diamonds in Fig. 10(b)].

Second, we find that the measured cross-correlation functions for a given horizontal velocity component (either v_x or v_y) but at different locations coincide with each other, suggesting that the velocity oscillations at different locations have the same phase relative to that of the temperature oscillation. This is possible only when the central region oscillates together as a whole. Third, the relative phase difference between the measured $C_x(\tau)$ and $C_y(\tau)$ is found to be zero, suggesting that the velocity oscillation in the central region is linearly polarized. Because the rms values of v_x or v_y are approximately the same [see Fig. 13(b) for more details], the oscillation direction should be along the bisectional line between the x and y axes.

Finally, we discuss the phase relation between the temperature oscillation and the horizontal velocity oscillation. From the recent temperature and velocity measurements,[13,14] we learned the mixing dynamics of the thermal plumes. As illustrated in Fig. 5, when the falling cold plumes arrive at the lower surface, heat exchange takes place mainly on the left side of the lower plate ($\sim 3L/4$ in size). At (almost) the same time, the impact of the cold plumes triggers off an instability of the lower thermal boundary layer, resulting in an eruption of warm plumes on the right-hand side of the lower plate ($\sim L/4$ in size). Because the strong mixing effect can locally stabilize the thermal boundary layer, the emission of warm plumes is suppressed in the region where the falling cold plumes are annihilated. A similar process takes place near the upper conducting surface after a delay time $t_0 = L/U$.

This dynamic process determines the phase relation between the cold plumes at position 7 and the resulting horizontal velocity fluctuation (say, δv_x). Suppose that the bulk fluid is pushed to the right when the cold plumes erupt from the upper-left corner of the cell. To calculate the relative phase lets further assume that the horizontal force produced by the eruption of the cold plumes takes a simple form $F_x(t) \sim \sin(2\pi f_0 t)$, where $f_0 = 1/(2t_0)$ is the frequency of the temperature oscillation. The temperature signals at position 7 then have the form $\delta T(t) \sim -\sin(2\pi f_0 t - \epsilon)$. Here a minus sign is introduced for the cold plumes ($\delta T(t) < 0$) and the initial phase ϵ ($\simeq 2\pi f_0 t_0/2 = \pi/2$) takes care of the delay time for the cold plumes to travel from the upper surface to position 7. The velocity signals in the central region can be obtained via $\delta v_x(t) = \int F_x(t')dt' \sim -\cos(2\pi f_0 t)$. Finally, the cross-correlation function can be written as $C_x(\tau) \sim \langle \delta T(t)\, \delta v_x(t+\tau)\rangle \sim \langle \sin(2\pi f_0 t - \epsilon)\cos[2\pi f_0 (t+\tau)]\rangle = -\cos(2\pi f_0 \tau)$.

It is seen from Figs. 9 and 10 that the calculated phase agrees with the measurements. Figures 9 and 10 thus suggest that the thermal plumes in the sidewall region interact with the fluid in the central region via the hydrodynamic forces, which introduce a phase shift to the horizontal velocity. We notice that the minimum (valley) position of the measured $C_x(\tau)$ and $C_y(\tau)$ is not exactly at $\tau = 0$ as calculated but is shifted by a small amount to the left. However, this shift is very small (~ 6 s) when compared with the oscillation period $1/f_0 \simeq 56$ s at Ra$=3.3\times10^9$. In the above calculation of the initial phase ϵ, we have ignored the time delay between the arrival of cold plumes and the emission of warm plumes at the lower conducting surface (and the similar delay time at the upper conducting surface). This small delay time has

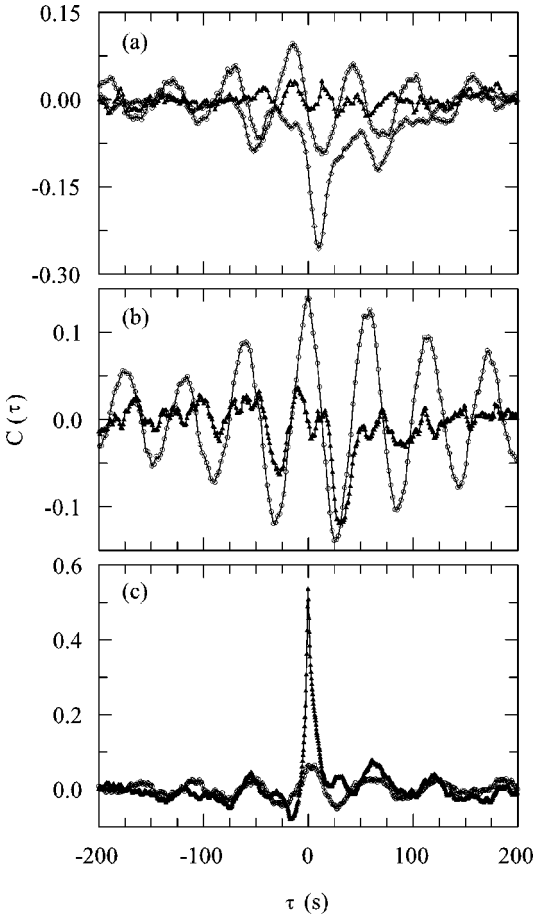

FIG. 11. Measured temperature–velocity cross-correlation functions $C_x(\tau)$ (open diamonds), $C_y(\tau)$ (open circles), and $C_z(\tau)$ (solid triangles) as a function of delay time τ at Ra$=3.3\times10^9$. In the experiment the temperature probe is fixed at position 7 and the velocity measurements are made at positions (a) 1 ($z=14$ mm), (b) 5 ($x=83$ mm), and (c) 7 ($x=-75$ mm). The lines are drawn to guide the eye.

been detected in a recent experiment[14] and may contribute to the small shift shown in Figs. 9 and 10.

The thermal plumes may also interact with the surrounding fluid through direct entrainment.[30,31] In this case, $\delta T(t)$ and δv_z will be in phase. Figure 11 shows the measured $C_x(\tau)$ (open diamonds), $C_y(\tau)$ (open circles), and $C_z(\tau)$ (solid triangles) when the velocity measurements are made at positions 1, 5, and 7. These are three typical locations around the cell periphery, in which the thermal plumes concentrate. It is seen from Fig. 11(c) that the vertical velocity near the sidewall indeed oscillates with the same phase as that of the temperature oscillation. Because of the direct entrainment by the cold plumes ($\delta T(t)<0$) at position 7, the nearby fluid has a downward velocity ($\delta v_z<0$). Consequently, the measured $C_z(\tau)$ peaks at $\tau=0$ with a large positive amplitude $C_z(0)\simeq0.54$. The correlation between $\delta T(t)$ and δv_z decays as the measuring position of δv_z is moved to the central region. At position 6, which is 2.8 cm away from position 7, the measured $C_z(0)$ is reduced to 0.094 [see Fig. 10(b)]. It is also found from Fig. 11(c) that the horizontal velocity δv_y at position 7 has the same phase as $\delta T(t)$ (and δv_z). The measured $C_y(\tau)$ peaks at $\tau=0$ but the correlation amplitude is small [$C_y(0)\simeq0.066$].

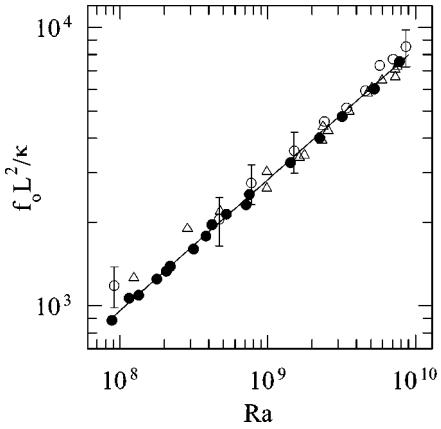

FIG. 12. Normalized oscillation frequency f_0L^2/κ obtained from the temperature power spectrum near the sidewall (solid circles), the power spectrum of the horizontal velocity v_x at the cell center (open circles), and the autocorrelation function of the horizontal velocity v_y near the sidewall (open triangles). The solid line is a power-law fit, $f_0L^2/\kappa=0.167\ \mathrm{Ra}^{0.47}$, to the solid circles.

At position 5 the velocity fluctuations δv_z and δv_y become in phase with the warm plumes, whose phase is opposite to that of the cold plumes at position 7. Because $\delta T(t)<0$, the resulting correlation functions $C_z(\tau)$ and $C_y(\tau)$ still peak at $\tau=0$. This is clearly shown in Fig. 11(b). At position 1 the horizontal velocity fluctuation δv_x is defined to be positive when its direction is the same as the large-scale flow and there is a time delay between δv_x and the cold plumes ($\delta T(t)<0$) at position 7. Therefore, the measured $C_x(\tau)$ becomes minimum near $\tau=0$ with the exact valley position shifted toward the right in an amount equal to the time for the cold plumes to travel from position 7 and position 1 [see Fig. 11(a)]. Similarly, $C_y(\tau)$ is found to be in phase with $C_x(\tau)$. Figure 11(a) also reveals that the correlation between $\delta T(t)$ and δv_z at position 1 is very small with $C_z(0)\simeq0.037$, which is at noise level.

C. Rayleigh number dependence

Figure 12 compares the measured velocity oscillation frequency with that of the temperature oscillation at different Rayleigh numbers. The solid circles show the normalized temperature oscillation frequency f_0L^2/κ obtained from the temperature power spectrum near the sidewall. This set of data is well described by the power law $f_0L^2/\kappa=0.167\ \mathrm{Ra}^{0.47}$ (solid line). This result is in good agreement with the recent temperature measurements in low temperature helium gas.[25] The open circles are the normalized velocity oscillation frequency obtained from the power spectrum of v_x at the cell center. The open triangles are obtained from the autocorrelation function of v_y near the sidewall. In the latter measurements, the bulk fluid temperature varied for less than 6 °C. As a result, the open triangles exhibit somewhat larger scatterer at lower Ra. It is seen from Fig. 12 that the velocity oscillation frequencies measured at different locations and obtained with different methods can all be superposed on a single master curve, which coincides with the temperature oscillation curve. Figure 12 thus demonstrates that the velocity and temperature oscillations are indeed

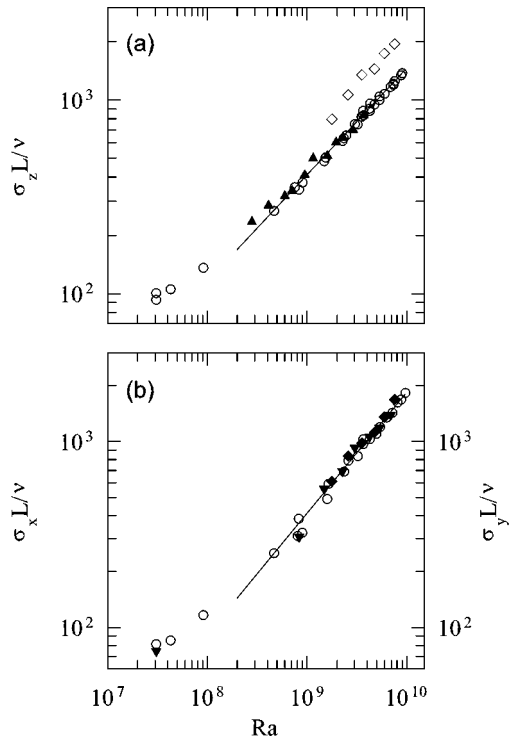

FIG. 13. (a) Normalized vertical rms velocity $\sigma_z L/\nu$ (open circles) as a function of Ra. The solid triangles are obtained by Daya and Ecke (Ref. 32). These velocity measurements are made at the center of the $A=1$ cells. The solid line is a power-law fit, $\sigma_z L/\nu = 4.6\times10^{-3}\ \mathrm{Ra}^{0.55}$, to the open circles at large Ra. The open diamonds are obtained near the sidewall. (b) Normalized horizontal rms velocities $\sigma_x L/\nu$ (open circles) and $\sigma_y L/\nu$ (solid triangles) as a function of Ra. The velocity measurements are made at the center of the $A=1$ cells. The solid line is a power-law fit, $\sigma_x L/\nu = 5.8\times10^{-4}\ \mathrm{Ra}^{0.65}$, to the open circles at large Ra. The solid diamonds are the measured $\sigma_y L/\nu$ near the sidewall.

driven by a common mechanism. As discussed above, both the velocity and temperature oscillations are generated by the alternating emission of thermal plumes between the upper and lower thermal boundary layers.

Besides the oscillation frequency, we also measure the Ra-dependence of the oscillation amplitude of the horizontal velocities and the vertical velocity fluctuations at the cell center. Figure 13(a) shows the normalized vertical rms velocity, $\sigma_z L/\nu$, as a function of Ra. Here σ_z is defined as $\sigma_z = [\langle (v_z - \overline{v_z})^2 \rangle]^{1/2}$. The open circles are obtained at the center of the $A=1$ cells and represent the best set of data we have to date. The time average for each data point runs for more than 8 h and the measurements are repeated many times over a period of 6 months. The data points in the Ra range, $3\times10^7 \leqslant \mathrm{Ra} \leqslant 5\times10^8$, are obtained in the smaller $A=1$ cell. Because the convective flow is slow, the measured rms values have a relatively larger error bar when compared with the mean values. The experimental uncertainties are mainly statistical and the relative error for σ_z is approximately 15%. This estimate is based on the scatterer of 1-h-long time-averaged rms values obtained from run to run. The solid triangles are obtained by Daya and Ecke in a different experiment.[32] Their data overlap with ours (open circles) well. Because there is no apparent oscillation for the vertical velocity at the cell center [see Fig. 3(c)], the measured σ_z represents the typical amplitude of vertical velocity fluctuations.

It is seen from Fig. 13(a) that the measured σ_z curves up in the entire Ra range, $3\times10^7 \leqslant \mathrm{Ra} \leqslant 9\times10^9$, and the data cannot be fitted to a single power law. Nevertheless, the velocity data measured in the larger $A=1$ cell with $\mathrm{Ra} > 7.6\times10^8$ can be well described by an effective power law, $\sigma_z L/\nu = 4.6\times10^{-3}\ \mathrm{Ra}^{\beta}$, with the exponent $\beta = 0.55\pm0.03$ (solid line). Because the data curve up at small Ra, the obtained value of β varies slightly depending on the Ra range used. For example, Daya and Ecke fitted their data with $\beta = 0.5$.[32] The value of β becomes slightly larger than 0.5 when the data points at larger Ra are included. We also measure σ_z in the sidewall region. It is seen from Fig. 13(a) that the measured σ_z near the sidewall (open diamonds) is 55% larger than that at the cell center. This result further supports our conclusion that the vertical velocity oscillation is driven by the thermal plumes near the sidewall through direct entrainment. Because the vertical shearing force starts from the sidewall region, the amplitude of the vertical rms velocity is expected to decay from the sidewall to the cell center.

Figure 13(b) shows the normalized horizontal rms velocities, $\sigma_x L/\nu$ (open circles) and $\sigma_y L/\nu$ (solid triangles), as a function of Ra. These velocity measurements are made at the center of the $A=1$ cells. The open circles have the same statistical accuracy as those shown in Fig. 13(a). The solid diamonds are the measured $\sigma_y L/\nu$ near the sidewall. Because there are strong oscillations in the horizontal directions (see Fig. 3), the measured σ_x and σ_y actually represent the oscillation amplitude of the horizontal velocities. It is seen from Fig. 13(b) that the measured rms values at different locations and along different directions are approximately the same, further confirming that the bulk fluid oscillates together as a whole in a horizontal direction. As discussed in Sec. III B, the horizontal velocity oscillation is linearly polarized and the polarization direction is along the bisectional line between the x and y axes, because the rms velocities in the two horizontal directions are equal ($\sigma_x \simeq \sigma_y$).

Similar to the situation for σ_z, the measured σ_x also curves up in the entire Ra range and cannot be fitted to a single power law. Nevertheless, the velocity data measured in the larger $A=1$ cell with $\mathrm{Ra} > 7.6\times10^8$ can be described by an effective power law, $\sigma_x L/\nu = 5.8\times10^{-4}\ \mathrm{Ra}^{\beta}$, with the exponent $\beta = 0.65\pm0.03$ (solid line). While it varies slightly depending on the Ra range used in the fitting, the obtained value of β for σ_x is certainly larger than that for σ_z ($\beta = 0.55\pm0.03$). Further comparison between Figs. 13(a) and 13(b) reveals that the two fitted solid lines for σ_x and σ_z cross each other at $\mathrm{Ra} \simeq 10^9$ and the value of σ_x becomes larger than σ_z at the high Ra end.

From the above velocity measurements at different locations and in cells of different aspect ratios, we find that the measured rms velocities at the cell center, where the mean velocity is zero, are influenced strongly by the large-scale motion. This is certainly true for the horizontal rms velocities. The bulk fluid in the central region oscillates together and therefore σ_x and σ_y measure the oscillation amplitude of the horizontal velocities. While there is no apparent oscillation found in the vertical velocity at the center of the $A=1$

cell, velocity fluctuations in the vertical direction can still be affected by the overall coherent motion in the region. Evidently, strong vertical velocity oscillations are found at the center of the $A=2$ cell. These measurements suggest that the oscillation of the velocity field is a response of the bulk fluid in a closed cell to the thermal forcing produced by the periodic emission of the thermal plumes near the conducting surfaces. Thus one expects that the velocity variations can be influenced considerably by the geometry of the cell, which determines the large-scale motion. In fact, Daya and Ecke[32] have found that the Ra-dependence of the measured σ_z at the cell center changes with the shape of the convection cell.

IV. SUMMARY

We have carried out a systematic study of the velocity oscillation in turbulent thermal convection. Simultaneous measurements of the local velocity and temperature are conducted in small aspect-ratio cells filled with water. From these measurements we obtain the temperature–velocity cross-correlation function and study the velocity oscillations over varying Rayleigh numbers and spatial positions across the entire cell. These structural measurements provide an interesting physical picture for the temperature and velocity oscillations in a closed cylindrical cell. The temperature oscillation is generated by the alternating emission of cold and warm plumes between the upper and lower thermal boundary layers. The cold and warm plumes are separated laterally in two opposing sidewall regions and exert buoyancy forces to the bulk fluid. An alternating eruption of the thermal plumes, therefore, gives rise to a periodic impulsive torque, which drives the large-scale circulation continuously.

The spatial organization of the thermal plumes produces a unique flow structure, which undergoes a coherent rotation. Careful examination of the measured temperature-velocity cross-correlation functions reveals that the thermal plumes interact with the convecting fluid in a closed cell in two different modes. First, they directly entrain the surrounding fluid in the sidewall region along the vertical direction. For example, when a warm plume is pushed away from the lower conducting surface by buoyancy, it entrains the surrounding fluid and pulls the nearby plumes towards it.[14] This ''hydrodynamic attraction'' causes the warm plumes and the surrounding fluid to move together, which explains why the vertical velocity oscillation occurs mainly in the plume-dominated sidewall region and its phase remains the same as that of the temperature oscillation.

Second, the interaction between the thermal plumes and the bulk fluid in the central region takes place via hydrodynamic forces, which introduce a phase shift to the two horizontal velocity components in the region. It is found that the velocity oscillation in the central region of the $A=1$ cell is predominantly in the horizontal direction. The horizontal velocity oscillation is linearly polarized and its phase is opposite to that of the temperature oscillation. The velocity oscillation frequency f_0 is found to be the same as that of the temperature oscillation and obeys the same power law, $f_0 L^2/\kappa = 0.167\ \mathrm{Ra}^{0.47}$, in the Ra range between 10^8 and 10^{10}.

The velocity oscillation in the central region of the $A=2$ cell is stronger and is observed in all three velocity components. Contrary to the situation in the $A=2$ and $A=1$ cells, no obvious velocity oscillation is observed in the $A=0.5$ cell. The large-scale flow in the $A=0.5$ cell is not stable, which may destroy the coherent stimulations needed for the generation of the temperature oscillation.[14] The velocity measurements conducted at different locations and in cells of different aspect ratios clearly show that the large-scale convective flow in a closed cell is influenced strongly by the cell geometry, such as the shape and the aspect ratio of the cell.

In wind tunnels and other open flow systems, the disturbance flow produced by the boundaries is confined in the near-wall region and is quickly discharged to the downstream. Because of these reasons the flow boundaries usually do not perturb the velocity fluctuations in the bulk region.[33] This situation is changed completely for flows in a closed cell, in which the disturbances produced by the boundaries are inevitably mixed into the turbulent bulk region. For example, we find that the measured rms velocities at the cell center are coupled directly to the large-scale motion in the closed convection cell.

While at the moment we do not have a theory to show quantitatively how the thermal plumes near the cell boundary produce horizontal velocity oscillations at the cell center, the experiment clearly reveals that the velocity oscillation is a response of the bulk fluid to the periodic emission of the thermal plumes between the upper and lower thermal boundary layers. Evidently the cell shape and aspect ratio can influence the spatial distribution and the dynamics of the thermal plumes, which may explain the observed geometry-dependence of temperature and velocity fluctuations at the cell center.[32] A further theoretical analysis is needed in order to fully understand the hydrodynamic interaction between the thermal plumes and the horizontal velocity oscillations in the central region. Clearly, the present experiment provides an interesting example to demonstrate how the thermal plumes organize themselves in a closed cell to generate a large-scale flow structure, which rotates and oscillates coherently in a turbulent environment.

ACKNOWLEDGMENTS

We thank L. Kadanoff, D. Lohse, R. Ecke, Z. Daya, and J. Niemela for useful discussions and communications. The assistance of M. Lucas and his team in fabricating the convection cells is gratefully acknowledged. P.T. was supported in part by the National Science Foundation under Grant No. DMR-0071323 and by the Research Grants Council of Hong Kong SAR under Grant No. HKUST 603003. K.-Q.X. was supported by the Research Grants Council of Hong Kong SAR under Grant No. CUHK4281/00P.

[1] B. Castaing, G. Gunaratne, F. Heslot, L. Kadanoff, A. Libchaber, S. Thomae, X.-Z. Wu, S. Zaleski, and G. Zanetti, ''Scaling of hard thermal turbulence in Rayleigh–Bénard convection,'' J. Fluid Mech. **204**, 1 (1989).
[2] E. Siggia, ''High Rayleigh number convection,'' Annu. Rev. Fluid Mech. **26**, 137 (1994).

[3]S. Grossmann and D. Lohse, ''Scaling in thermal convection: A unifying theory,'' J. Fluid Mech. **407**, 27 (2000).
[4]L. P. Kadanoff, ''Turbulent heat flow: Structures and scaling,'' Phys. Today **54** (8), 34 (2001).
[5]M. Sano, X.-Z. Wu, and A. Libchaber, ''Turbulence in helium-gas free convection,'' Phys. Rev. A **40**, 6421 (1989).
[6]S. Ashkenazi and V. Steinberg, ''High Rayleigh number turbulent convection in a gas near the gas-liquid critical point,'' Phys. Rev. Lett. **83**, 3641 (1999); ''Spectra and statistics of velocity and temperature fluctuations in turbulent convection,'' *ibid.* **83**, 4760 (1999).
[7]X.-L. Qiu, S. H. Yao, and P. Tong, ''Large-scale coherent rotation and oscillation in turbulent thermal convection,'' Phys. Rev. E **61**, R6075 (2000).
[8]X.-D. Shang and K.-Q. Xia, ''Scaling of the velocity power spectra in turbulent thermal convection,'' Phys. Rev. E **64**, 065301(R) (2001).
[9]T. Takeshita, T. Segawa, J. G. Glazier, and M. Sano, ''Thermal turbulence in mercury,'' Phys. Rev. Lett. **76**, 1465 (1996).
[10]S. Cioni, S. Ciliberto, and J. Sommeria, ''Strongly turbulent Rayleigh–Bénard convection in mercury: Comparison with results at moderate Prandtl number,'' J. Fluid Mech. **335**, 111 (1997).
[11]S. Ciliberto, S. Cioni, and C. Laroche, ''Large-scale flow properties of turbulent thermal convection,'' Phys. Rev. E **54**, R5901 (1996).
[12]E. Villermaux, ''Memory-induced low frequency oscillations in closed convection boxes,'' Phys. Rev. Lett. **75**, 4618 (1995).
[13]X.-L. Qiu and P. Tong, ''Large-scale velocity structures in turbulent thermal convection,'' Phys. Rev. E **64**, 036304 (2001).
[14]X.-L. Qiu and P. Tong, ''Temperature oscillations in turbulent Rayleigh–Bénard convection,'' Phys. Rev. E **66**, 026308 (2002).
[15]X. Chavanne, F. Chilla, B. Castaing, B. Hebral, B. Chabaud, and J. Chaussy, ''Observation of the ultimate regime in Rayleigh–Bénard convection,'' Phys. Rev. Lett. **79**, 3648 (1997); X. Chavanne, F. Chilla, B. Chabaud, B. Castaing, and B. Hebral, ''Turbulent Rayleigh–Bénard convection in gaseous and liquid He,'' Phys. Fluids **13**, 1300 (2001).
[16]J. J. Niemela, L. Skrbek, K. R. Sreenivasan, and R. J. Donnelly, ''Turbulent convection at very high Rayleigh numbers,'' Nature (London) **404**, 837 (2000).
[17]X. Xu, K. M. Bajaj, and G. Ahlers, ''Heat transport in turbulent Rayleigh–Bénard convection,'' Phys. Rev. Lett. **84**, 4357 (2000).
[18]G. Ahlers and X. Xu, ''Prandtl-number dependence of heat transport in turbulent Rayleigh–Bénard convection,'' Phys. Rev. Lett. **86**, 3320 (2001).
[19]K.-Q. Xia, S. Lam, and S.-Q. Zhou, ''Heat-flux measurement in high-Prandtl-number turbulent Rayleigh–Bénard convection,'' Phys. Rev. Lett. **88**, 064501 (2002).
[20]X.-L. Qiu and P. Tong, ''Onset of coherent oscillations in turbulent Rayleigh–Bénard convection,'' Phys. Rev. Lett. **87**, 094501 (2001).
[21]X.-Z. Wu and A. Libchaber, ''Non-Boussinesq effects in free thermal convection,'' Phys. Rev. A **43**, 2833 (1991).
[22]J. Zhang, S. Childress, and A. Libchaber, ''Non-Boussinesq effect: Thermal convection with broken symmetry,'' Phys. Fluids **9**, 1034 (1997).
[23]L. E. Drain, *The Laser Doppler Technique* (Wiley, New York, 1980).
[24]S.-L. Lui and K.-Q. Xia, ''Spatial structure of the thermal boundary layer in turbulent convection,'' Phys. Rev. E **57**, 5494 (1998).
[25]J. J. Niemela, L. Skrbek, K. R. Sreenivasan, and R. J. Donnelly, ''The wind in confined thermal convection,'' J. Fluid Mech. **449**, 169 (2001).
[26]K. R. Sreenivasan, A. Bershadskii, and J. J. Niemela, ''Mean wind and its reversal in thermal convection,'' Phys. Rev. E **65**, 056306 (2002).
[27]X.-Z. Wu and A. Libchaber, ''Scaling relations in thermal turbulence: The aspect-ratio dependence,'' Phys. Rev. A **45**, 842 (1992).
[28]R. Verzicco and R. Camussi, ''Numerical experiments on strongly turbulent thermal convection in a slender cylindrical cell,'' J. Fluid Mech. **477**, 19 (2003).
[29]P.-E. Roche, B. Castaing, B. Chabaud, and B. Hebral, ''Prandtl and Rayleigh number dependence in Rayleigh–Bénard convection,'' Europhys. Lett. **58**, 693 (2002).
[30]J. S. Turner, ''Turbulent entrainment: The development of the entrainment assumption and its application to geophysical flows,'' J. Fluid Mech. **173**, 431 (1986).
[31]E. Moses, G. Zocchi, and A. Libchaber, ''An experimental study of laminar plumes,'' J. Fluid Mech. **251**, 581 (1993).
[32]Z. A. Daya and R. E. Ecke, ''Does turbulent convection feel the shape of the container?'' Phys. Rev. Lett. **87**, 184501 (2001).
[33]H. Tennekes and J. L. Lumley, *A First Course in Turbulence* (MIT Press, Cambridge, 1972).